Geochemistry Geophysics Geosystems G3

Article
Volume 13, Number 3
8 March 2012
Q03007, doi:10.1029/2011GC003994
ISSN: 1525-2027

Published by AGU and the Geochemical Society

Experiments on upward migration of a liquid-rich layer in a granular medium: Implications for a crystalline magma chamber

Yasuko Shibano
Graduate School of Natural Science and Technology, Kanazawa University, Kakuma, Kanazawa 920-1192, Japan

Atsuko Namiki
Department of Earth and Planetary Science, University of Tokyo, 7-3-1, Hongo, Bunkyo, Tokyo 113-0033, Japan (namiki@eps.s.u-tokyo.ac.jp)

Ikuro Sumita
Graduate School of Natural Science and Technology, Kanazawa University, Kakuma, Kanazawa 920-1192, Japan

[1] We perform a series of experiments to investigate the situation in which a melt-rich layer formed by a magma intrusion ascends through a crystalline magma chamber. The initial condition is such that a heavier granular layer overlies a liquid layer. The particles consisting the upper granular layer are in a jammed state, and only the particles near the interface can move to form a dilated boundary layer. The dilated layer detaches from the upper granular layer, and forms downwelling plumes which drive a cellular convection within the liquid-rich layer. The convection erodes the upper granular layer, and the liquid-rich layer migrates upwards with time. This upward migration of the liquid-rich layer differs from the previously known mechanisms of liquid transport; permeable flow in which the liquid migrates at the Darcy velocity, the Stokes settling in which the individual particle settles, and diapirs formed by the Rayleigh-Taylor instability. We find that the velocity of the upward migration of the liquid-rich layer can be scaled by the volumetric flux of the liquid ascending through the narrow channel between the particles. The upward migration of the liquid-rich layer is faster than the Darcy velocity. In a mushy magma chamber whose crystals are in a jammed state, neither the Stokes settling nor the Rayleigh-Taylor instability can occur. We propose that the upward migration of the melt-rich layer observed in our experiments can become an efficient mechanism of melt transport in a crystalline magma chamber.

Components: 9800 words, 7 figures, 1 table.

Keywords: convection; dilation; granular media; magma chamber; melt transport; reactivation.

Index Terms: 3618 Mineralogy and Petrology: Magma chamber processes (1036); 3643 Mineralogy and Petrology: Layered magma chambers; 5114 Physical Properties of Rocks: Permeability and porosity.

Received 5 December 2011; **Revised** 31 January 2012; **Accepted** 4 February 2012; **Published** 8 March 2012.

Shibano, Y., A. Namiki, and I. Sumita (2012), Experiments on upward migration of a liquid-rich layer in a granular medium: Implications for a crystalline magma chamber, *Geochem. Geophys. Geosyst.*, *13*, Q03007, doi:10.1029/2011GC003994.

1. Introduction

[2] Reactivation of a magma chamber by the intrusion of a more mafic magma has been suggested at several volcanoes [e.g., *Pallister et al.*, 1992; *Nakamura*, 1995; *Murphy et al.*, 2000; *Couch et al.*, 2001; *Bachmann et al.*, 2002]. Petrological observations of andesitic lava erupted at the Soufriére Hills volcano, Montserrat, indicate the presence of a heating event and the intermingling of crystals suggests that convection within the magma layer occurred [*Murphy et al.*, 2000; *Couch et al.*, 2001]. Similar remobilization and convection within the magma layer has been suggested for the Fish Canyon magma in Colorado [*Bachmann et al.*, 2002].

[3] Since a solidifying magma is polycrystalline [e.g., *Ghiorso et al.*, 2002], the melt is distributed along the grain boundaries. The rheology of such a solid–liquid mixture depends strongly on its crystallinity [*Lejeune and Richet*, 1995; *Costa*, 2005; *Caricchi et al.*, 2007; *Walsh and Saar*, 2008; *Ishibashi*, 2009]. When the crystallinity is close to the maximum packing volume fraction, solid grains jam each other and become immobile.

[4] Measured crystallinity of the lava at Soufriére Hills volcano, Montserrat, is 45–55% [*Murphy et al.*, 2000], and that for the Fish Canyon magma is 40–45% [*Bachmann et al.*, 2002]. These values are close to the maximum volumetric solid fraction in which the mobility of the grains is severely limited [e.g., *Saar et al.*, 2001]. Since the crystallinity of the erupted lava corresponds to that after the reactivation event, the crystallinity in the mushy magma chamber before the reactivation is possibly higher than the measured one. The mushy magma may be immobile. The estimate of the energy balance indicates that the injection of a new magma alone cannot explain the reactivation of midsize and large crystal mushes [*Huber et al.*, 2010].

[5] On the other hand, convection within the magma chamber has been investigated by several previous works. *Huppert and Sparks* [1988] conduct experiments using waxes and aqueous solutions having different densities, to model the process of basaltic magma intruding into the continental crust which results in the roof melting. Eutectic system can make another melt layer between the roof and the intruding magma [*Kaneko and Koyaguchi*, 2000]. The intruding magma can also melt the sidewalls [*Leitch*, 2004].

[6] The melt-rich layer generated by the magma intrusion is less dense than the overlying crystalline mush. If the Rayleigh-Taylor (gravitational) instability occurs between the melt-rich layer and the overlying highly crystalline layer, it can provide an explanation for the petrologically observed remobilization and convection within the magma chamber [*Burgisser and Bergantz*, 2011]. It is however not obvious whether the immobile-crystalline mushes can deform sufficiently fast to cause the Rayleigh-Taylor instability from the buoyancy of the melt-rich layer alone.

[7] Even when the crystals in the mush are in a jammed state, crystals near the interface with a melt-rich region is mobile [e.g., *Forterre and Pouliquen*, 2008]. An experiment of the Rayleigh-Taylor instability between a close-packed granular layer and a liquid layer shows that, when the roof consists of a particle-jammed layer, only the lower most part of the jammed layer becomes mobile and descends [*Michioka and Sumita*, 2005]. *Huber et al.* [2011] suggest that internal overpressurization of the mush induced by small amounts of melting makes microfractures around the interface between the crystalline mush and the melt-rich layer, and breaks the crystalline framework. The fractured region may descend before the whole crystalline layer deforms. The particle settling in the magma chamber has also been investigated previously [*Martin and Nokes*, 1989; *Koyaguchi et al.*, 1990; *Huppert et al.*, 1991]. However, whether such a liquid layer can ascend through the thick jammed layer remains unsolved. In order to understand the melt transport in a reheated magma chamber, we should know how the grains close to the jammed state become mobile and how the unlocked grains descend into the melt-rich layer.

[8] In this paper we report a series of experiments to clarify how a liquid-rich layer ascends through a granular layer in which the particles are in a jammed state. From the experiments, we find that the descending particles organize themselves into plumes which drive a cellular convection pattern within the liquid layer. The granular layer is gradually being eroded by the convection and the liquid-rich layer migrates upwards as time progresses. This is different from the classic Rayleigh-Taylor instability for the superimposed layers of miscible liquids. Based upon the experiments, we construct a scaling law which explains the velocity of the

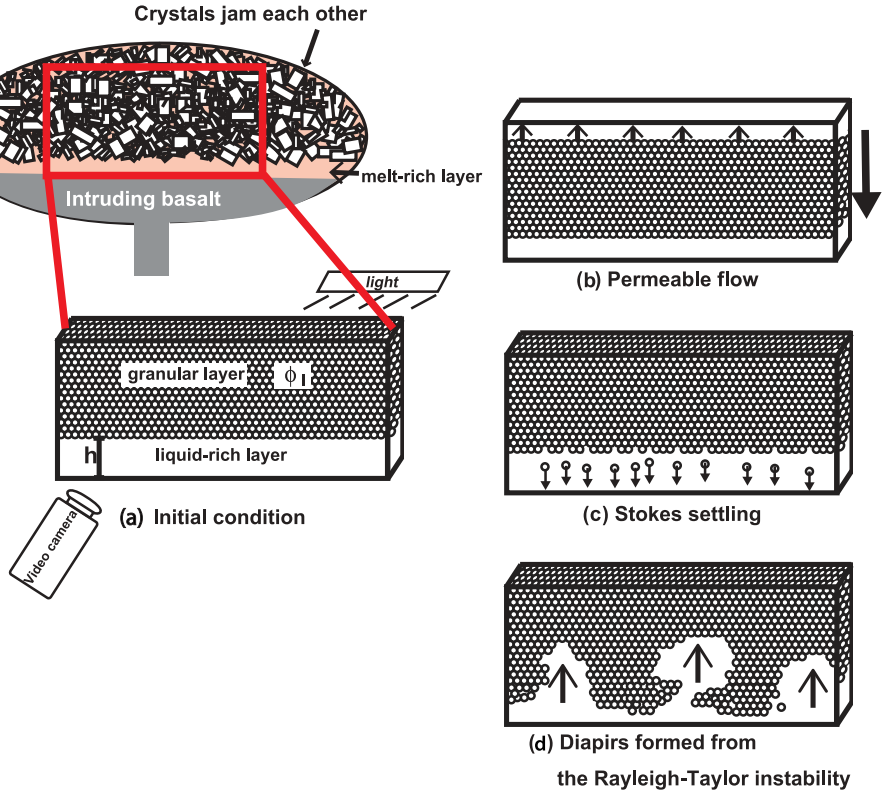

Figure 1. (a) A schematic diagram of the initial condition of the experiments and the corresponding situation in the magma chamber. (b–d) The possible mechanisms to transport the liquid-rich layer based on the previous works.

upward migration of the liquid-rich layer, and apply the scaling to the crystalline magma chamber.

2. Experimental Method

[9] Experimental procedure is as follows. First, we leave a tank filled with a specified fraction of glass beads, ϕ_{ms}, and silicone oil to allow the glass beads to settle. Next, we quickly invert the tank upside down to attain the initial condition as shown in Figure 1a. We observe the flow pattern of the beads and record them by a digital video camera with a resolution of 1980 × 1080 pixels at 30 frames per second. For the case in which the flow is slow, we use a digital camera with a resolution of 3648 × 2736 pixels at 1 frame per 5 s.

[10] We varied the initial thickness of the liquid-rich layer h which is related to the mean volume fraction of the glass beads ϕ_{ms}, liquid viscosity μ, and bead radius a. Details of the experimental parameters are listed in Table 1. Beads radii have ranges around their mean values, 0.025 ± 0.0065, 0.11 ± 0.020, 0.31 ± 0.063 mm whose densities are ρ_s = 2500, 2450, and 2500 kg m^{-3}, respectively. The liquid density is ρ_l = 970 kg m^{-3}. In most of the experiments, we invert the same tank 4 times under similar waiting times to confirm the reproducibility of the results. In Table 1, the experiments with the same ϕ_{ms} and tank size indicates that the same tank is used. In our experiments, we use spherical glass beads. The experimental tank is illuminated from behind by a linear halogen light source which is passed through an unwoven fabric in order to uniformly illuminate the tank. Here the granular layer appears as a dark region and the liquid-rich layer appears as a bright region. For some experiments, we have also illuminated the tank from the front (e.g., Figure 2e), and for this case, the glass beads appear grayish. Using different methods of lighting does not affect the observed phenomena, suggesting that there are no significant differences of the flow pattern depending on the distance from the tank wall.

[11] The images are analyzed using MATLAB by introducing a threshold brightness to define the boundary between the upper granular layer and the liquid-rich layer. In some experiments, a fraction of the descending particles are being suspended in the liquid-rich layer and the interface becomes increasingly blurred as time proceeds. For such cases, we

Table 1. A Summary of the Experiments and Their Parameters[a]

Viscosity (Pa s)	Initial h (mm)	Waiting Time (day)	ϕ_l	ϕ_s	ϕ_{ms}	Radius (mm)	Tank Size (mm mm mm)	Figure
0.49	8.0	7	0.36	0.64	0.53	0.11	45 × 170 × 9	Figure 4a
0.49	8.6	7.5	0.35	0.65	0.53	0.11	45 × 170 × 9	Figure 4a
0.49	9.4	7.5	0.33	0.67	0.53	0.11	45 × 170 × 9	Figures 2a, 4a, and 4b
0.49	9.5	7.5	0.33	0.67	0.53	0.11	45 × 170 × 9	Figure 4a
0.49	4.1	7	0.37	0.63	0.57	0.11	45 × 170 × 9	Figure 4a
0.49	4.9	8	0.36	0.64	0.57	0.11	45 × 170 × 9	Figure 4a
0.49	4.7	7.5	0.36	0.64	0.57	0.11	45 × 170 × 9	Figure 4a
0.49	4.7	7.5	0.36	0.64	0.57	0.11	45 × 170 × 9	Figures 2b and 4a
0.49	12.6	7	0.5*	0.5*	0.4*	0.11	45 × 170 × 9	Figure 4a
0.49	15.0	6	0.5*	0.5*	0.4*	0.11	45 × 170 × 9	Figure 4a
0.49	15.9	12	0.4*	0.6*	0.4*	0.11	45 × 170 × 9	Figure 4a
0.49	15.5	7.5	0.5*	0.5*	0.4*	0.11	45 × 170 × 9	Figure 4a
0.49	1.9	7	0.38	0.62	0.59	0.11	45 × 170 × 9	Figure 4a
0.49	2.3	7.5	0.38	0.62	0.59	0.11	45 × 170 × 9	Figure 4a
0.49	1.3	7	0.39	0.61	0.59	0.11	45 × 170 × 9	Figure 4a
0.49	1.6	7	0.38	0.62	0.59	0.11	45 × 170 × 9	Figure 4a
0.097	10.0	4.5	0.42	0.58	0.45	0.11	45 × 170 × 9	Figure 2c
0.097	10.4	4	0.41	0.59	0.45	0.11	45 × 170 × 9	
0.097	11.2	4	0.40	0.60	0.45	0.11	45 × 170 × 9	
0.097	10.3	4	0.41	0.59	0.45	0.11	45 × 170 × 9	
0.097	6.8	4.5	0.4*	0.6*	0.5*	0.11	45 × 170 × 9	
0.097	6.0	4	0.4*	0.6*	0.5*	0.11	45 × 170 × 9	
0.097	6.3	4	0.4*	0.6*	0.5*	0.11	45 × 170 × 9	
0.097	6.0	4	0.4*	0.6*	0.5*	0.11	45 × 170 × 9	
0.097	1.4	4.5	0.39	0.61	0.59	0.11	45 × 170 × 9	
0.097	1.7	4	0.39	0.61	0.59	0.11	45 × 170 × 9	
0.097	1.4	4	0.39	0.61	0.59	0.11	45 × 170 × 9	
0.097	1.4	4	0.39	0.61	0.59	0.11	45 × 170 × 9	
0.097	3.0	4	0.4*	0.6*	0.6*	0.11	45 × 170 × 9	
0.097	2.6	4.5	0.4*	0.6*	0.6*	0.11	45 × 170 × 9	
0.097	3.2	4.5	0.4*	0.6*	0.6*	0.11	45 × 170 × 9	
0.097	2.9	4.5	0.4*	0.6*	0.6*	0.11	45 × 170 × 9	
0.097	7.0	5	0.40	0.60	0.50	0.11	45 × 170 × 9	
0.097	6.4	4.5	0.41	0.59	0.50	0.11	45 × 170 × 9	
0.097	12.8	5	0.37	0.63	0.53	0.31	82 × 122 × 15	Figure 2d
0.097	7.7	5	0.40	0.60	0.54	0.31	79 × 172 × 28	
0.097	20.6	5	0.39	0.61	0.46	0.025	82 × 122 × 15	Figure 2e
0.49	7.1	7	0.41	0.59	0.57	0.11	179 × 179 × 10	Figures 3a and 4b
0.49	7.3	7	0.41	0.59	0.57	0.11	179 × 179 × 10	Figure 4b
0.49	9.4	7	0.40	0.60	0.57	0.11	179 × 179 × 10	Figures 3b and 4b
0.49	8.2	7	0.41	0.59	0.57	0.11	179 × 179 × 10	Figure 4b

[a]Each column indicates liquid viscosity, initial thickness of the liquid-rich layer (h), waiting time allowed for the particles to settle prior to inverting the cell, liquid fraction in the upper granular layer (ϕ_l), solid fraction in the upper granular layer (ϕ_s), average solid fraction in the tank (ϕ_{ms}), particle radius, inner dimensions of the tank, and the corresponding figure numbers in which the experimental results are shown. Asterisks indicate that accuracy of ϕs is limited. See text for details.

track its height only until the time in which the interface appears clear. The particles eventually settle at the bottom of the tank to form a sediment layer. We do not analyze the interface between the newly formed sediment layer and the liquid-rich layer, because this interface is also blurred.

[12] We calculate the initial solid fraction of the upper granular layer from $\phi_s = (\rho - \rho_l)/(\rho_s - \rho_l)$, where subscripts s and l correspond to solid and liquid, respectively, ρ is the mixture density of the upper granular layer which is calculated from the total mass M, tank volume V, the measured thickness of the liquid-rich layer h, and the upper granular layer l as $\rho = \{M - \rho_l Vh/(l + h)\}/\{Vl/(l + h)\}$. The initial liquid fraction in the upper granular layer can then be calculated from $\phi_l = 1 - \phi_s$. The thickness h cannot be measured to a precision of less than 1 mm which results in an uncertainty of the liquid fraction of < 0.02. The inner tank volume can be calculated from the mass of the beads and the oil. In some experiments denoted by asterisks in

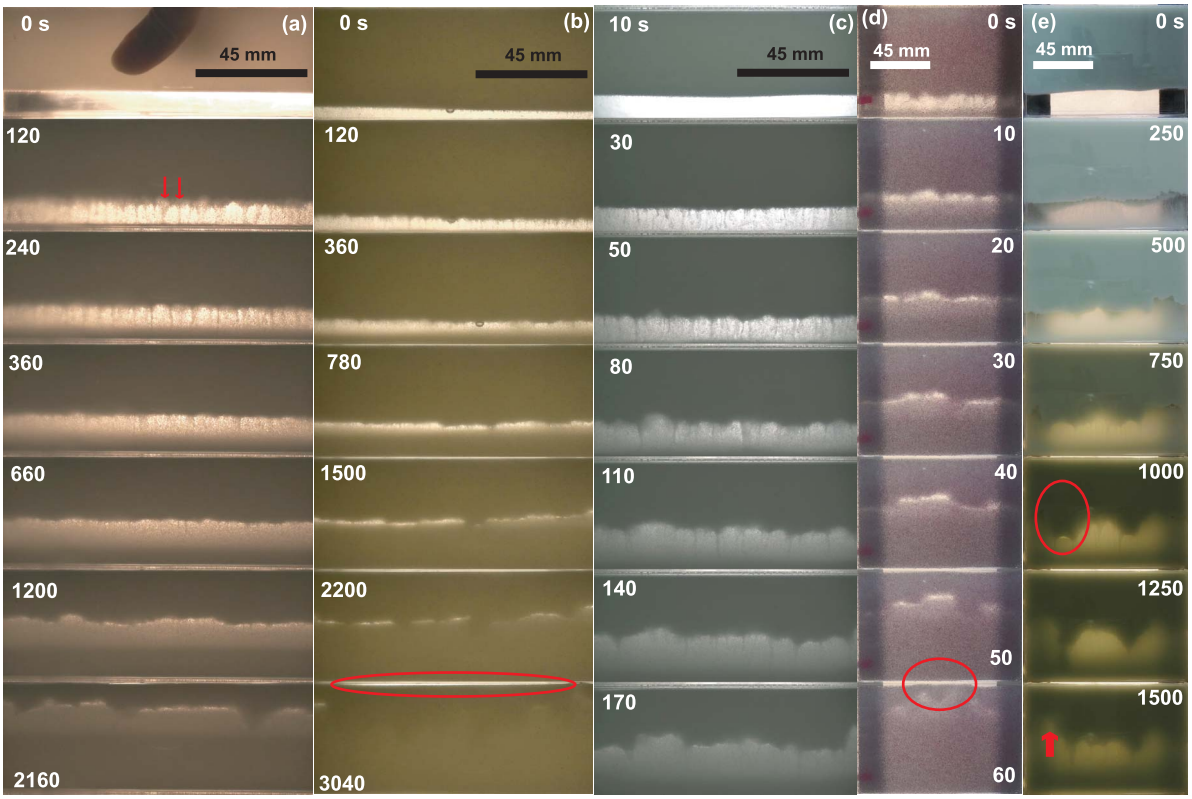

Figure 2. Images of the liquid-rich layer ascending through the upper granular layer. See Table 1 for the details of the parameters. The brighter region corresponds to the region with a large liquid fraction. Numbers indicate the time elapsed after the tank is inverted. (a) Standard case with a liquid viscosity of 0.49 Pa·s, thickness of the liquid-rich layer of 9.4 mm, and a bead radius of 0.11 mm. (b) The case for a thinner liquid-rich layer of 4.7 mm. (c) The case for a smaller liquid viscosity of 0.097 Pa·s. (d) The case for a larger particle radius 0.31 mm, and a liquid viscosity of 0.097 Pa·s. (e) The case for a smaller particle radius 0.025 mm, and a liquid viscosity of 0.097 Pa·s. The variation of color contrasts in these figures mainly arises from the difference of the methods used for illumination. In Figure 2e, 0–500 s, the tank is illuminated from the front. In Figures 2d and 2e, the dark regions at the both ends are the double-faced tapes used to anchor the tank. In Figure 2d, pink beads are mixed with the white beads.

Table 1, these are not measured and we use the volume of another tank measured by filling water. The tank which we use is commercially supplied and the volume difference between each tank is estimated to be less than 10%.

3. Possible Mechanisms of Liquid Transportation

[13] For our experimental situation, previous fluid mechanical studies suggest that the following 3 mechanisms are candidates of liquid transportation: i.e., (1) permeable flow, (2) Stokes settling, and (3) diapirs formed from the Rayleigh-Taylor instability, which we show schematically in Figure 1.

[14] First, we consider permeable flow (Figure 1b) in which the buoyant liquid ascends through the interstitial granular space. As the liquid rises, the whole granular layer slides downward as a counter flow. For this case, the volumetric flow per unit area (Darcy velocity) can be expressed as

$$q = \frac{k}{\mu}\Delta\rho(1-\phi_l)g, \tag{1}$$

where k is permeability, $\Delta\rho = \rho_s - \rho_l$, is the density difference between the solid and liquid, g is the gravitational acceleration, and μ is the liquid viscosity. For the permeability k, we use the Kozeny-Carman equation [e.g., *Carman*, 1937; *Bear*, 1972]

$$k = \frac{a^2}{k'}\frac{\phi_l^3}{(1-\phi_l)^2} \tag{2}$$

where a is the particle radius, and k' is an empirical constant which depends on the shape of the particles. The flow velocity of the liquid becomes q/ϕ_l. *Carman* [1937] compiles experimentally measured

k' and concludes that a value of $k' \sim 45$ is suitable for uniform spherical particles. *Maaløe and Scheie* [1982] deform the glass spheres and measure permeability at lower liquid fractions ($0.05 < \phi_l < 0.25$) and *McKenzie* [1984] calculates an appropriate value to fit their measurements to obtain $k' \sim 1000$. In this study, we use $k' \sim 45$ to calculate the permeability, since we use spherical beads in our experiments.

[15] Second mechanism is the Stokes settling (Figure 1c). When the individual particles at the bottom of the upper granular layer descend through the liquid-rich layer, the liquid-rich layer migrates upwards as a counter flow. The descending velocity of a single particle can be estimated using the Stokes velocity

$$v_s \sim \frac{2}{9}\frac{\Delta\rho g a^2}{\mu}. \tag{3}$$

In a suspension, particles settle slower than the Stokes velocity because of the viscous interaction between the adjacent particles. This is known as the hindered settling, and can be expressed as a function of liquid fraction [*Davis and Birdsell*, 1988; *Huppert et al.*, 1991]

$$v_h = \phi_l^5 v_s. \tag{4}$$

[16] Third mechanism is the fluid transport by diapirs which forms as a consequence of the Rayleigh-Taylor instability (Figure 1d). The Rayleigh-Taylor instability occurs if the upper granular layer deforms similar to a viscous fluid. For viscous fluids, it is known that the undulation of the interface initially grows exponentially as a function of elapsed time t ($\propto \exp(nt)$). The growth rate n of the interface undulation scales with the thickness of the liquid-rich layer h [e.g., *Selig*, 1965; *Whitehead and Luther*, 1975]

$$n \propto \frac{(\rho - \rho_l)gh}{\eta}\left(\frac{\mu}{\eta}\right)^{1/3}, \tag{5}$$

where ρ is the density of the upper granular layer, h is the thickness of the lower liquid-rich layer, and η is the effective viscosity of the upper granular layer.

[17] The effective viscosity of a dense granular media can be expressed using an empirical formula, Krieger-Dougherty equation [e.g., *Krieger and Dougherty*, 1959],

$$\frac{\eta}{\mu} = \left(1 - \frac{\phi_s}{\phi_{sc}}\right)^{-m}, \tag{6}$$

where m is a constant in the range of $1.5 < m < 5$, ϕ_{sc} is the volume fraction of the solid particles when the particle packing is maximum. The value for the random close packing fraction of uniform spheres is around $\phi_{sc} = 0.635$ [e.g., *Onoda and Liniger*, 1990; *Mavko et al.*, 1998]. According to equation (6), the effective viscosity of the close packed upper granular layer becomes infinitely large for our initial condition. Therefore, the timescale for the growth of the undulation becomes quite long. This is because the particles are in a jammed state and the granular media cannot deform. In reality, even a dense granular media shows finite viscosity because of particle rearrangement. *Costa* [2005] and his comment (http://arxiv.org/abs/physics/0512173) provide a modified form of equation (6),

$$\frac{\eta}{\mu} = \frac{1 + \left(\frac{\phi_s}{\phi_{max}}\right)^{\beta}}{\left(1 - \alpha \mathrm{erf}\left\{\frac{\sqrt{\pi}}{2\alpha}\frac{\phi_s}{\phi_{max}}\left[1 + \left(\frac{\phi_s}{\phi_{max}}\right)^{\gamma}\right]\right\}\right)^{2.5\phi_{max}}}. \tag{7}$$

Caricchi et al. [2007] calculate the empirical relations between the shear rate and the fitting parameters ϕ_{max}, α, β, γ.

[18] If the undulation grows to form low viscosity diapirs, their ascending velocity can be estimated by

$$v_d \sim \frac{1}{3}\frac{(\rho_o - \rho_i)gR^2}{\eta}, \tag{8}$$

where $\rho_o - \rho_i$ is the density difference of the fluids outside and inside of the diapir. Here the size of the diapir R which has formed from the Rayleigh-Taylor instability should be scaled by the thickness of the liquid-rich layer $R \sim h$. Since the effective viscosity η of the close packed upper granular layer is quite large, the ascending velocity of the diapir is also slow.

[19] Differences of the particle size and the liquid fraction of the granular layer affect which mechanism operates to transport the liquid. When the upper layer consists of a dilute suspension of fine solid particles or immiscible liquids, we may approximate the upper layer as a homogeneous fluid having a larger effective viscosity compared to the suspending fluid. For such case, Rayleigh-Taylor type instability occurs, whose characteristic growth rate and wavelength can be explained by applying the theories formulated assuming viscous fluids [*Voltz et al.*, 2001; *Olson and Weeraratne*, 2008].

[20] *Bagdassarov et al.* [1996] experimentally study the gravitational instability for the situation in which platinum powders overlie a partially molten granite, and show that both Stokes settling and

Rayleigh-Taylor type instabilities are possible, depending on the parameters which control the velocity of these two instabilities. *Deubelbeiss et al.* [2010] conduct a 2-D numerical calculation of the gravitational instability for the case in which the polyhedral particles consist the upper granular layer. They also show that the Stokes settling and the Rayleigh-Taylor instability are possible and obtain the conditions under which these two types are realized.

[21] When the upper granular layer is close packed, none of the above mechanisms may work. *Michioka and Sumita* [2005] show that a limited region near the interface with the liquid-rich layer dilates to become mobile, to form descending plumes. Similar plumes are also observed in the experiments with bubbles and in numerical experiments with particles [*Thomas et al.*, 1993; *Bergantz and Ni*, 1999]. We call this type of instability as "partial instability." *Michioka and Sumita* [2005] study the initial stages of the partial instability when the thin upper granular layer overlies a thick liquid layer. The question of how a liquid-rich layer ascends through a thick granular layer remains unanswered.

[22] *Vinningland et al.* [2007] perform experiments with a thick granular layer and air, and show that the plumes which consist of several particles continuously emerge and the air layer ascends through the upper granular layer. The air layer eventually separates into several pockets. However, it is not obvious whether similar phenomena occur in a viscous fluid. Finally, *Rabinowicz et al.* [2001] numerically study how the melt layer ascends through the compacting partially molten medium and show that the layer migrates upwards maintaining its sill-like shape which sometimes becomes melt pockets. In their calculations, however, the motion of individual particles is not taken into account.

4. Results

4.1. Qualitative Features of the Upward Migration of the Liquid-Rich Layer

[23] Figure 2a and Animation S1 show an experimental result for the case with a liquid-rich layer thickness of h = 9.4 mm, waiting time to invert the tank of 7.5 days, liquid fraction in the granular layer of ϕ_l = 0.33, and a liquid viscosity of 0.49 Pa·s.[1] This value of liquid fraction is smaller than that for random close packing, ∼ 0.365 [e.g., *Onoda and Liniger*, 1990; *Mavko et al.*, 1998], suggesting that the granular layer is in a jammed state.

[24] At 0 s immediately after the tank is inverted, the interface between the upper granular layer and the bottom liquid-rich layer remains flat. After 20 s, the interface moves downward indicating the dilation of the granular layer. Thereafter the glass beads start to fall at locations approximately equally spaced to form descending plumes as shown by the red arrows in Figure 2a. The initial stages of the instability described above are the same as that observed by *Michioka and Sumita* [2005].

[25] An important finding from the present experiments is that this phenomenon continues and evolves as we describe below. In the liquid-rich layer, the descending plumes drive cellular convection and a counter upwelling flow is observed. As time elapses, the downwelling plumes which are adjacent to each other coalesce and the plume spacing gradually increases. The glass beads which consist the downwelling plumes eventually settle at the base of the tank. As a result, after ∼ 240 s, a three-layered structure becomes evident, which consists of a bottom granular layer, a middle liquid-rich layer and a top granular layer. As time proceeds, the downwelling plumes continually erode the interface and the thickness of the upper granular layer decreases. The liquid-rich layer thus migrates upwards maintaining its sill-like shape. The particle concentration within the liquid-rich layer increases with time as is evident from the image at 2160 s. The convection within the middle liquid-rich layer becomes increasingly sluggish, as a consequence of the increase in effective viscosity. We have conducted the experiment using the same tank 4 times and obtained essentially the same result.

[26] None of the 3 mechanisms which we summarize in Figure 1 accurately describe the above phenomena. After the particles begin descending to form a dilated layer, the particles quickly organize themselves into plumes. Only the particles near the interface with the liquid-rich layer are involved in the instability, and therefore differs from the image shown in Figure 1d, in which the whole granular layer deforms. In addition, the plumes consisting of several particles drive cellular convection which is also different from the Rayleigh-Taylor instability of viscous fluids. Note that since the convection is driven by downwelling plumes, it resembles the convection pattern driven by internal heating in which a thermal boundary layer forms at the top boundary only and descending plumes form. This is also similar to the convection driven by bubbles

[1] Auxiliary materials are available in the HTML. doi:10.1029/2011GC003994.

that are continuously supplied from the bottom [*Iga and Kimura*, 2007].

4.2. Effects of the Liquid-Rich Layer Thickness, Fluid Viscosity and Particle Size

[27] Figure 2b and Animation S2 show the case for a thinner liquid-rich layer h (= 4.7 mm) compared to the case shown in Figure 2a. Similar to Figure 2a, as time proceeds, the liquid-rich layer migrates upwards. The widths of the individual plume observed in Figure 2b are similar to those observed in Figure 2a, but the widths of the convection cells in the liquid-rich layer are smaller such that the aspect ratio of the cells remain similar. This is another feature resembling thermal convection. At 1500 s, the downwelling plume and the bottom granular layer become connected such that the liquid-rich layer is separated into several pockets with small particle concentration. The number of liquid-rich pockets increases with time, and finally the liquid-rich layer disappears at 3040 s. On the other hand, a clear liquid-rich layer appears at the top of the tank as indicated by a red circle. This layer should have formed from a permeable flow accompanied by the downward sliding of the jammed granular layer, as we show schematically in Figure 1b.

[28] We also vary the liquid viscosity (Figure 2c and Animation S3) and particle radius (Figures 2d and 2e and Animations S4 and S5), and confirm that the same phenomena occurs; i.e., the liquid-rich layer migrates upwards accompanied by an internal convection. We confirm that when the liquid viscosity becomes smaller (Figure 2c), the upward migration velocity becomes faster.

[29] Similarly, we find that the upward migration velocity scales with the particle size; i.e., faster for a larger particle size (Figure 2d), and slower for a smaller particle size (Figure 2e). In the case for large particles (Figure 2d), the liquid finally erupts out at the top, forming a distinct topography as indicated by a red circle. In the case for smaller particles (Figure 2e), undulation of the interface between the liquid-rich layer and the upper granular layer becomes larger compared to the case for a larger particle size. Aggregates of the particles exceeding the size of the individual plumes intermittently descend as indicated by a red circle and an arrow. As a consequence, the migration velocity of the liquid-rich layer is found to fluctuate with time.

4.3. Long-Term Evolution

[30] In order to investigate the long term evolution of the flow pattern, we conduct experiments using a larger tank (Figure 3 and Animations S6 and S7). Apart from the initial thickness of the granular layer, the conditions are similar to the case shown in Figure 2a. Here two experimental runs with the same total content of the solid particles are shown. In both Figures 3a and 3b, the granular plumes descend from the interface, and the interface migrates upward with time, which is similar to those observed in Figure 2a. The intermittent descending of large aggregates of the particles as shown in Figure 2e is also observed.

[31] As time proceeds, we observe a difference between Figures 3a and 3b. The undulation of the interface grows rapidly with time for Figure 3a compared to Figure 3b. In Figure 3a, a liquid-rich blob forms at $t \sim 3510$ s which rises by eroding the surrounding granular layer. The eroded particles descend along the wall of the granular region. The shape of the liquid-rich region is diapir-like but its ascending mechanism is different from that for the diapir observed in the viscous fluid in which the diapir ascends by the deformation of the surrounding fluid.

[32] On the other hand, in Figure 3b a sill-like shape persists longer, and the fluid migrates at a slower velocity compared to Figure 3a. The above comparison indicates that the upward migration velocity depends on the shape of the liquid-rich region; a region with a diapiric shape ascends faster than the region with a sill-like shape.

[33] We also note that a liquid-rich layer appears at the top of the tank after 3510 s in Figure 3a and 5610 s in Figure 3b, similar to that observed in Figure 2b. This indicates that the permeable flow and the downward sliding of the granular layer as shown in Figure 1b is occurring at the same time.

[34] The observed features in our experiments are similar to those observed in the study by *Vinningland et al.* [2007], in which the interparticle fluid is air. *Vinningland et al.* [2007] show that the air layer migrates upwards by forming plumes which consist of particles around the interface. The air layer eventually becomes several pockets. The upper granular layer slides downward.

4.4. Time Evolution of the Interface

[35] Figure 4a shows how the average height of the interface migrates upwards with time for the experiments with the same viscosity 0.49 Pa·s, particle radius 0.11 mm, but with the different initial thickness of the liquid-rich layer (Table 1), as indicated by the different colors and different

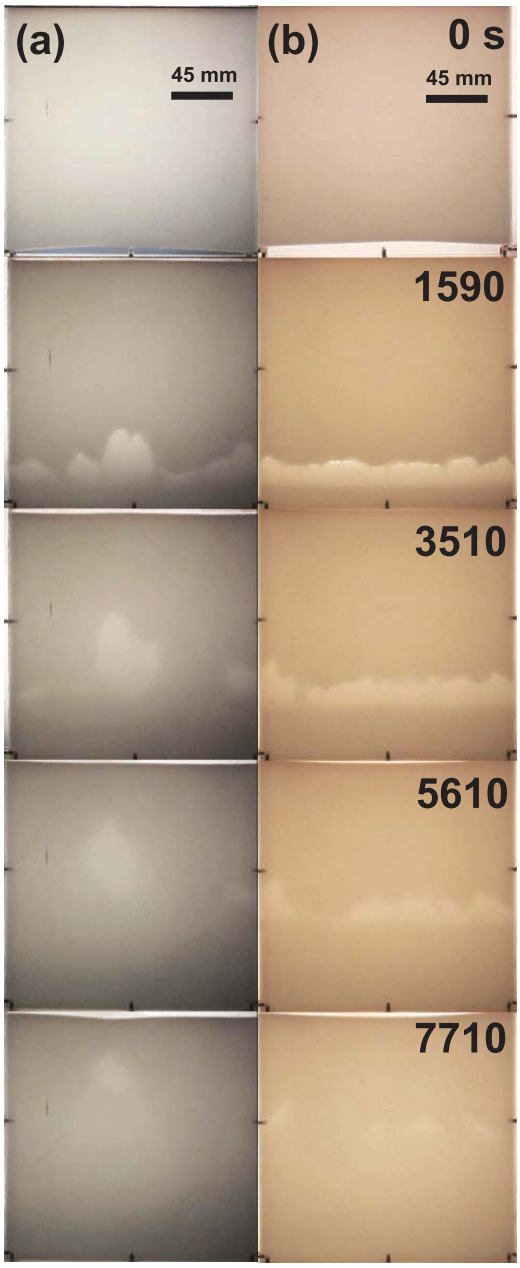

Figure 3. Images of the liquid-rich layer ascending through the granular medium for a longer vertical distance (179 mm). Numbers indicate the time elapsed after the tank is inverted. See Table 1 for the details of the parameters.

starting heights at $t = 0$. The error bars indicate the maximum and minimum heights, which correspond to the amplitude of the undulation. The slopes which correspond to the migration velocity, are approximately constant at least until 1000 s and do not depend on the initial thickness of the liquid-rich layer.

[36] The possible mechanisms of the upward transport of the liquid-rich layer which we summarized in Figure 1 are permeable flow, which results in the sliding down of the granular layer at the Darcy velocity (Figure 1b), the Stokes settling (Figure 1c), and diapirs which have been pinched off by the Rayleigh-Taylor instability (Figure 1d). Comparison shows that the upward migration velocity is smaller than the Stokes velocity, equation (3), 8×10^{-2} mm s^{-1}, as indicated by a thin line, but faster than the Darcy velocity, equation (1), 4×10^{-4} mm s^{-1}, as indicated by a thick line. Experiments show that the measured upward migration velocity does not depend on the initial thickness of the liquid-rich layer (Figure 4a). This is different from the characteristics of diapirs formed from the Rayleigh-Taylor instability. Growth rates of the Rayleigh-Taylor instability, equation (5), and the velocity of the diapir, equation (8), are scaled with the initial thickness of the liquid-rich layer h, since diapir radius R depends on h [e.g., *Whitehead and Luther*, 1975]. In addition, unlike the Rayleigh-Taylor instability of viscous fluids, the undulation of the interface does not fully develop as is evident from the approximately constant length of the error bars in Figure 4a. Therefore, neither of the above 3 mechanisms sufficiently explain the upward migration of the liquid-rich layer.

[37] Figure 4b shows the maximum height of the liquid-rich layer, which increases with time, for the experiments shown in Figure 3. The migration velocity of the interface for different runs is similar as is evident from the close overlap of the height data until $\sim$ 1000 s. However, variations of the height growth among the different runs become evident after $\sim$ 1000 s. The experimental runs shown by the curves in green and light blue are the cases in which the liquid-rich layer remains horizontal throughout the experiment in the form of a sill. The ascending velocity is close to the data plotted by blue diamonds which corresponds to the case shown in Figure 2a. On the other hand, the experimental runs shown by red and pink curves are the cases in which the liquid-rich layer finally becomes a diapir which results in a faster ascent rate. This indicates that the upward migration velocity can be modified depending on the shape of the interface.

[38] In Figure 4b, we also plot the minimum height of the interface between the granular layer and the newly formed liquid-rich layer at the top of the tank. For comparison, we calculate the Darcy velocity, equation (1), as indicated by a black line which shows a good agreement with the experiments. We therefore interpret the appearance of a new liquid-rich layer at the top of the tank as a

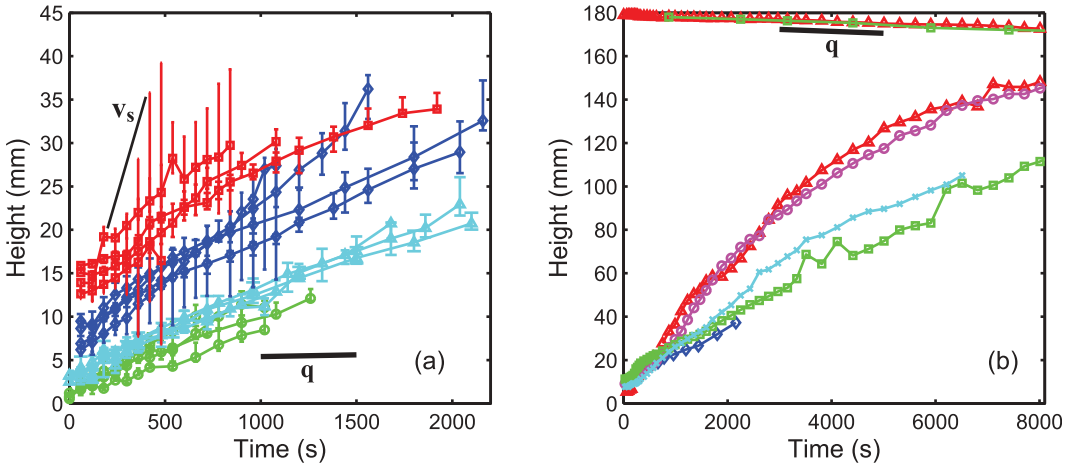

Figure 4. (a) Average heights of the interface as a function of time after the tank is inverted for the experiments with different initial thickness of the liquid-rich layer. Apart from the initial thickness, other parameters are similar to those for the case shown in Figure 2a. Experiments conducted with the same tank which has similar initial thickness of the liquid-rich layer are plotted using the same color and symbols. Error bars indicate the maximum and minimum heights of the interface. Slope of the thick black line labeled q corresponds to the Darcy velocity calculated using equation (1). The slope of the thin black line labeled v_s corresponds to the Stokes velocity calculated using equation (3). (b) Heights of the interface between the granular layer and the liquid-rich layer as a function of time for the experiments conducted in the large tank as shown in Figure 3. The data points which increase with time correspond to the maximum height of the ascending liquid-rich layer. The data points which decrease with time correspond to the minimum height of the newly formed liquid-rich layer at the top of the tank. The marker colors (red, pink, green, light blue) correspond to those of the experiments in the order tabulated in Table 1 (the lowermost 4 cases). The data points in blue correspond to the experiment shown in Figure 2a. A thick black line labeled q is the Darcy velocity estimated using equation (1) and $\phi_1 = 0.4$.

consequence of the laterally homogeneous permeable flow as we have shown schematically in Figure 1b. The fact that the downward sliding of the upper granular layer is scaled by the Darcy velocity indicates that localized channels observed in the soluble porous media [e.g., *Kelemen et al.*, 1995] do not develop in our experiments.

[39] Note that the liquid in the new layer at the top does not come from the initial liquid-rich layer at the bottom, but originates from the inter-granular liquid. Such permeable flow will accompany downward sliding of the whole granular layer. However, apart from the initial dilation stage, the initial liquid-rich layer is found to migrate upwards with time. This indicates that in our experiments, the permeable flow has only a secondary role in the liquid transport.

5. Discussion

[40] Figure 5a compares the measured upward migration velocities with those estimated using 4 different velocity models. Here we calculate the velocity from the slope shown in Figure 4a during the time span in which the liquid-rich layer migrates upwards maintaining its sill-like shape and a cellular convection develops within the liquid-rich layer. For the case in which aggregates of the particles intermittently descend (Figure 2e), we average the velocity before such intermittent descending commences. We only plot the experiments in which the initial liquid fraction ϕ_1 are accurately measured which correspond to those without asterisks in Table 1. The black line with a slope of 1 is a reference line indicating that the measured and the calculated velocities agree. Green, blue, pink markers indicate Stokes, equation (3), Darcy, equation (1), and hindered settling velocities, equation (4), respectively. Comparison shows that the measured upward migration velocity is slower than the Stokes settling velocity, and faster than the hindered settling and Darcy velocities.

[41] Red markers are calculated using the following model (Figure 5b), and agree best with the measured velocity. Dilation of the granular layer implies that the interparticle distance gradually increases and that there is an upward flow of the liquid into the increased space between the particles

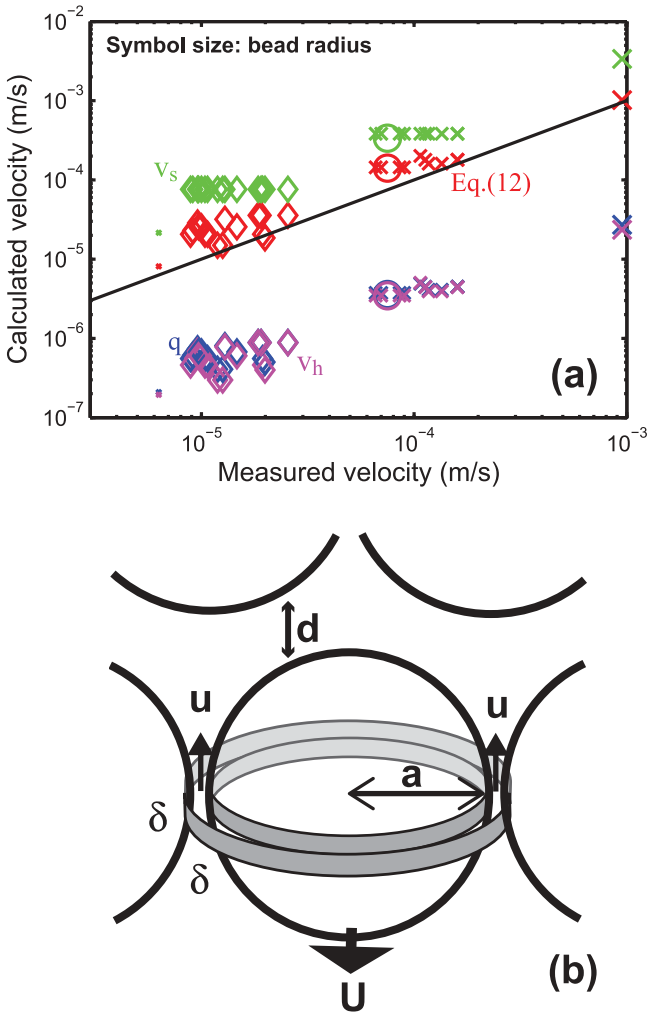

Figure 5. (a) Comparison of the measured and calculated upward migration velocities of the liquid-rich layer. The symbols ×, ◇, and ○ correspond to the case for the liquid viscosity of 0.097, 0.49, and 0.97 Pa·s, respectively. Difference of the symbol size represents the bead radius. The colors indicate the different methods used to estimate the velocities; i.e., red is calculated by the model shown in Figure 5b and equation (12), blue is the Darcy velocity q, equation (1), calculated using the liquid fraction in the granular layer (ϕ_l), green is the Stokes velocity v_s, equation (3), and pink is hindered settling velocity v_h, equation (4). The black line with a slope of 1 is shown as a reference and indicates that the measured and calculated velocities are equal. (b) A schematic diagram showing the descending of a particle at the bottom of the granular layer, and the upward counter flow through the annular region.

[e.g., *Davis et al.*, 1989]. When particles descend at a velocity U, the required volumetric flux of the liquid becomes $\pi a^2 U$. The liquid flows upwards through the narrow channel between the particles. We assume that this narrow channel is modeled as an annulus whose width and length is averaged liquid thickness δ. We can approximate δ by [*Princen et al.*, 1980; *Proussevitch et al.*, 1993]

$$1 - \phi_l = \left(\frac{a}{a + \delta/2}\right)^3. \tag{9}$$

Upward volumetric flux of the liquid through the annulus balances the downward volumetric flux of the particles. Since adjacent particles share the annulus, we approximate the half of the volumetric-liquid flux through the annulus is used to descend one particle

$$\pi a^2 U = \pi a \delta \frac{\delta^2}{12\mu} \frac{\Delta p}{\delta}. \tag{10}$$

The pressure difference arising from the negative buoyancy of the particle can be estimated from

$\Delta p = 4\pi\Delta\rho g a^3/(3\pi a^2)$. As a result, the descending velocity of the particle is estimated as

$$U = \frac{1}{9}\frac{\Delta\rho g\delta^2}{\mu}. \quad (11)$$

Michioka and Sumita [2005] have shown that when the liquid fraction of the dilated layer becomes $\phi_l = 0.58$, partial instability which causes the detachment of the dilated layer commences. This corresponds to $d/a = 0.7$ where d is the interparticle distance. Accordingly, we infer that after the timescale in which the dilation causes the interparticle distance to increase by $d = 0.7a$, partial instability occurs, and the bottom of the granular layer migrates upwards by a length scale of $2a$. Since this timescale becomes $(0.7a - \delta)/U$, the velocity scale becomes

$$\frac{2U}{0.7 - \delta/a} \quad (12)$$

which are shown by the red markers in Figure 5a.

[42] Since the red markers are closest to the black line, we conclude that our model shown in Figure 5b best explains the upward migration of the liquid-rich layer which is accompanied by internal convection.

6. Geological Implications

[43] Our experiments suggest a new image of liquid transport within the Earth; when the upper polycrystalline granular layer is in a jammed state, the underlying liquid-rich layer migrates upwards by eroding the upper granular layer maintaining its sill-like shape. Eventually the liquid-rich region forms a diapiric shape, and it migrates upwards continuously eroding the granular layer without deforming the whole granular layer.

[44] We apply our experimental results to a crystal-rich magma chamber in which the crystals jam each other. When a fresh magma intrudes and reheats the overlying immobile crystalline mush, the crystals around the interface melt and form a melt-rich layer which becomes mobile [*Burgisser and Bergantz*, 2011]. Under such a situation, two types of melts form; one is that consisting the melt-rich layer and the other is the suspending melt in the crystalline mush layer. Here we assume that these melts have similar density and are miscible with each other. The suspending melt coats each crystal. This situation is similar to the initial condition of our experiments (Figure 1a). Our experiments are conducted with a liquid having a lower viscosity and smaller particles compared to the actual magmatic melt and crystals. However, in all experiments, Reynolds number estimated by the Stokes velocity of the particle settling becomes $\mathrm{Re} = \rho_s\Delta\rho g a^3/\mu^2 \ll 1$, indicating that viscous stress overwhelm the inertial stress. This is consistent with the condition in a silicic magma chamber, since crystal sizes in the magma chamber is $<10^{-2}$ m, and melt viscosity is > 100 Pa·s. In our experiments, the ratio of gravitational to Brownian forces is greater than unity, $\Delta\rho g a^4/(k_B T) \gg 1$, where k_B is Boltzmann's constant and T is temperature. This is also consistent with the condition in the magma chamber. Our scaling in equation (12) based on our experiments is thus applicable to the phenomena within the magma chamber.

[45] In section 3, we summarized several possible mechanisms of melt transport. The permeable flow velocity, equation (1), and hindered settling velocity, equation (4), are slower than the measured upward migration velocity of the melt-rich layer (Figure 5a). Stokes settling, equation (3) does not occur in our experiments, and accordingly, we do not consider its possibility here. This is because when crystals in the magma chamber are in a jammed state, individual crystals cannot descend in the form of Stokes settling. We therefore compare the upward migration velocity, equation (12) with the diapiric ascent rate, equation (8).

[46] Figure 6 compares the estimated upward migration velocities (red and blue lines) with the diapiric ascent rate (green curves) in a crystalline magma chamber. In order to estimate the velocities, we assume the following conditions. The initial thicknesses of the melt-rich layers which become the radii of the diapirs are 0.1, 1, 10 m. The crystal radii are 2, 10 mm. The radius 2 mm approximately corresponds to the size of the largest phenocrysts in the magma of Unzen volcano which are supposedly to have been reheated [e.g., *Nakamura*, 1995; *Nakada and Motomura*, 1999]. The density difference between the crystals and the suspending melt is 300 kg m^{-3} [e.g., *Geschwind and Rutherford*, 1995]. This density difference corresponds to that between plagioclase and melt, and is a minimum estimate. The viscosity of the suspending melt is assumed to be 10^4 Pa·s corresponding to the andesitic to dacitic melt at around 900°C [e.g., *Takeuchi*, 2011]. The viscosity of the melt-rich layer is assumed to be 10^4 (blue dotted lines) and 10^2 Pa·s (red lines). The former is the same as that of suspending melt in a crystalline mush. The latter implies that the temperature within the melt-rich

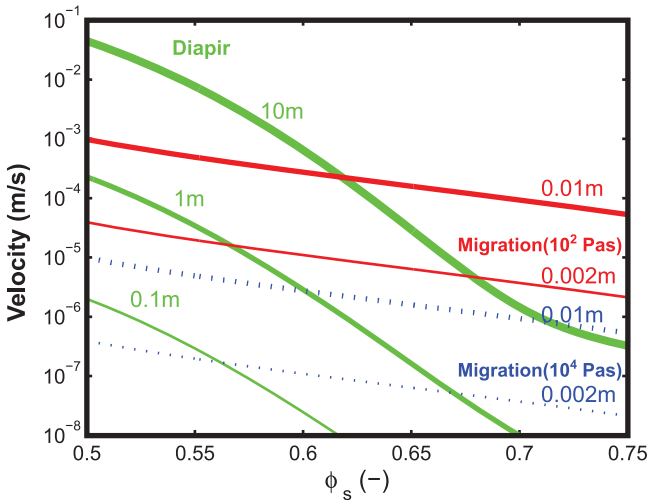

Figure 6. Estimated velocities as a function of solid fraction ϕ_s. Red solid and blue dotted lines indicate the upward migration velocity of a liquid-rich layer accompanied by the internal convection as observed in our experiments estimated by equation (12) assuming a melt viscosity of 10^2 and 10^4 Pa·s respectively. The thicknesses of the lines indicate the radii of crystals, 10^{-2}, 2×10^{-3} m, and are thicker for larger crystals. The green curves show the ascending velocities of diapirs with radii of 0.1, 1, 10 m estimated by equation (8), in which the effective viscosity of the granular layer is estimated by equation (7). Here we assume that the viscosity of the suspending melt of 10^4 Pa·s, and the density difference between crystals and melt of 300 kg m^{-3}.

layer is higher than that in the crystalline mush by about 200°C. This corresponds to the situation where the melt layer is in contact with the newly intruded hot basalt.

[47] The effective viscosity of the granular layer is calculated by equation (7), in which the fitting parameters, ϕ_{max}, α, β, γ, depend on the shear rate [*Caricchi et al.*, 2007]. Shear rate should be calculated using the diapiric ascent rate in equation (8) and the diapir radius, v_d/h. However, we do not know the effective viscosity in the crystalline mush and therefore we cannot estimate the shear rate. Accordingly, we assume the mush viscosity of 10^9 Pa·s to calculate the shear rate, which is close to the viscosity near the jammed state obtained from equation (6).

[48] Figure 6 shows that the upward migration velocity (red and blue lines) has a weaker dependence on the solid fraction compared to the diapiric ascent rate (green curves). This is due to a strong dependence of the effective viscosity on the solid fraction, equations (6) and (7). Diapiric ascent rate depends on the inverse of the effective viscosity, equation (8), whereas the upward migration velocity, equation (12), is independent of the effective viscosity. Figure 6 also shows that the diapiric ascent rate depends on the melt-rich layer thickness, equation (8), whereas the upward migration velocity is independent of the melt-rich layer thickness. As a result, when the solid fraction in the mush is high and the thickness of the melt-rich layer is thin, the upward migration velocity of the melt-rich layer overwhelms that of the diapiric ascent and therefore becomes an efficient mechanism of melt transport.

[49] The relative magnitude between the upward migration velocity and the diapiric ascent rate depends on the viscosity in the melt-rich layer and the crystal size. The upward migration velocity becomes faster as the phenocryst size becomes larger and the viscosity of the melt-rich layer becomes smaller.

[50] Based upon the characteristics of these velocities, we propose the following scenario of magma ascent. When the melt-rich layer is initially thin (<0.1 m) and the solid fraction of the overlying mush $\phi_s > 0.55$, the upward migration of the melt-rich layer occurs, because it is faster than the diapiric ascent. At this stage, the interface between the melt-rich layer and the crystalline mush dilates and descending plumes form (Figure 7). The phenocrysts descend through the melt-rich layer and settle above the basaltic layer or descend through the basaltic layer (Figure 1). When some phenocrysts remain in the melt-rich layer (Figure 3) or descend through the basaltic layer, the thickness of the melt-rich layer increases as time elapses. Even when the length scale of the melt-rich region becomes as thick as 10 m (green thick curve), the upward migration velocity is still faster than the diapiric

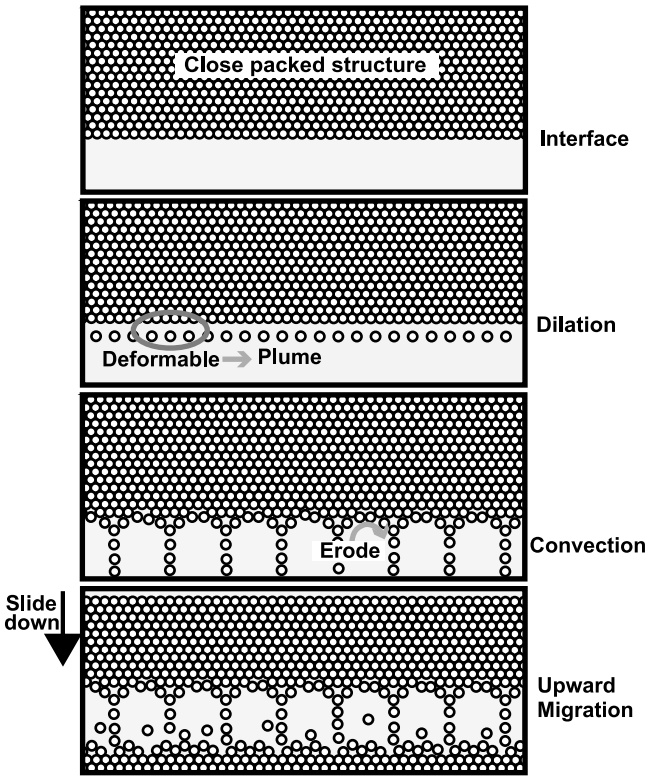

Figure 7. A schematic diagram showing the essential features of the experiments in which the liquid-rich layer migrates upwards accompanied by an internal convection.

ascent velocity if the melt-rich region remains hot enough such that the viscosity is around 10^2 Pa·s (red lines). The melt-rich layer eventually may become round in shape but ascends by the upward migration as shown in Figure 3a.

[51] After the melt-rich region is separated from the hot basalt and entrains cold phenocrysts, it becomes cold and the viscosity will rise. The upward migration of the melt-rich region (blue dotted thin line) becomes slower than the diapiric ascent rate (green thick curve). At this stage, the melt-rich layer may ascend as a diapir by deforming the surrounding mush [e.g., *Burgisser and Bergantz*, 2011].

[52] If there are size and density variation of the phenocrysts, small or light phenocrysts will not settle and remain suspended in the melt. The melt-rich region will thus contain phenocrysts which have originated from different parts of the mush. Variation of originated location of the phenocrysts can explain the intermingling within the magma chamber [*Murphy et al.*, 2000; *Couch et al.*, 2001].

[53] Phenocrysts, which keeps on growing in the magma chamber long before the reheating event, is expected to become large. Indeed, the observed phenocrysts in the magma of the Unzen volcano and Fish canyon which are supposed to have been reheated is quite large with a size of up to 5 mm [e.g., *Nakada and Motomura*, 1999; *Bachmann et al.*, 2002]. We infer that this is the largest size which can be suspended by the internal convection of the melt-rich layer. If there exist larger phenocrysts in the mush, the upward migration of the melt-rich layer will become faster (red thick line). If particles make aggregates [e.g., *Nakada and Motomura*, 1999] or blocks are generated from microfracturing [*Huber et al.*, 2011], aggregates or blocks will behave as large individual particles, and will also accelerate the upward migration velocity (Figure 2e).

[54] Our experiments are performed with spherical particles although the actual phenocrysts are polyhedral in shape. In our scaling, equation (12), the critical melt fraction above which the partial instability occurs is taken as $\phi_1 = 0.58$. If the shape of the phenocryst is prolate or oblate, the critical melt fraction for the partial instability to occur becomes larger [e.g., *Saar et al.*, 2001; *Walsh and Saar*, 2008]. On the other hand, the magma viscosity under the same melt fraction becomes larger compared to the spherical case [*Ishibashi*, 2009]. The non-spherical shape of the phenocrysts thus affects

both the thresholds for the whole mushy layer deformation and the partial instability similarly. We infer that the basic features of the flow remain unchanged even though the shape of the phenocrysts modifies the quantitative values of the thresholds which are used to calculate Figure 6. Accordingly, we consider that regardless of the shape of the phenocrysts, there exist a regime where the phenocrysts around the interface descend as plumes before the whole mushy layer deforms, resulting in the upward migration of the melt-rich layer.

[55] Another finding in our experiments is that a new liquid-rich layer appears at the top of the tank which has formed from a permeable flow accompanied by the downward sliding of the jammed granular layer, as we show schematically in Figure 1b. *Bachmann and Bergantz* [2004] have suggested that crystal-poor rhyolites are extracted from batholithic crystal mushes. *Masotta et al.* [2012] experimentally confirm that thermally zoned environment can make crystal-poor, differentiated magma above a crystalline mushy layer. As the mechanisms for causing these differentiations, hindered settling and compaction has been suggested. Sliding down of the whole mushy layer which we observed in our experiments, may also contribute to extract rhyolitic magmas.

[56] When a basaltic magma intrudes beneath a silicic magma chamber, the density of the basaltic magma is similar to or lighter than that of the crystals but is heavier than the inter-granular melt. If there is no silicic melt layer between the basaltic magma and the crystalline mush, both the upward migration and the Rayleigh-Taylor instability do not occur. Instead, the whole mushy layer can slide down.

[57] If the crystal-poor rhyolites are generated by the extraction process, the typical thickness of the rhyolite melt layer before the eruption is estimated as 500 m [*Bachmann and Bergantz*, 2004]. Assuming the permeability of silicic mushes as 10^{-8} m^2 [*Bachmann and Bergantz*, 2004], and the physical properties used in Figure 6, the timescale to form a 500 m thick crystal-poor melt layer is estimated as 10^4 years which is shorter than the residence time of the silicic mushes $>10^5$ years [*Bachmann and Bergantz*, 2004]. We thus infer that the downward sliding of the mushy layer can contribute to extract the crystal-poor rhyolites.

7. Conclusions

[58] We have conducted a series of experiments to investigate how a liquid-rich layer ascends through a close packed granular medium and have found that it ascends maintaining its sill-like shape as shown schematically in Figure 7. This is because the particles which consist the granular layer are in a random close packed state and only the particles near the interface can become mobile to form a loose boundary layer. This boundary layer becomes gravitationally unstable and detaches to form downwelling plumes which are accompanied by counter upwelling flow such that the liquid-rich layer convects. The granular layer is being continually eroded, and by repeating this process, the liquid-rich layer migrates upwards. Simultaneously, the granular layer slides downward and a new liquid-rich layer appears at the top of the granular layer by permeable flow. The upward migration velocity can be scaled by the volumetric flux of the liquid through the thin liquid film between the particles as shown in Figure 5b. In the crystalline magma chamber, this upward migration of the melt-rich layer can become an important mechanism to disintegrate the jammed crystals and transport melt.

Acknowledgments

[59] We thank T. Morishita for helpful discussion. Part of this work was supported by Grants-in-Aid for Scientific Research, JSPS (21244071, 22109505).

References

Bachmann, O., and G. W. Bergantz (2004), On the origin of crystal-poor rhyolites: Extracted from batholithic crystal mushes, *J. Petrol.*, *45*, 1565–1582.

Bachmann, O., M. A. Dungan, and P. W. Lipman (2002), The Fish Canyon magma body, San Juan volcanic field, Colorado: Rejuvenation and eruption of an upper-crustal batholith, *J. Petrol.*, *43*, 1469–1503.

Bagdassarov, N. S., A. M. Dorfman, and D. B. Dingwell (1996), Modeling of melt segregation processes by high-temperature centrifuging of partially molten granites—II. Rayleigh-Taylor instability and sedimentation, *Geophys. J. Int.*, *127*, 627–634.

Bear, J. (1972), *Dynamics of Fluids in Porous Media*, Dover, New York.

Bergantz, G. W., and J. Ni (1999), A numerical study of sedimentation by dripping instabilities in viscous fuids, *Int. J. Multiphase Flow*, *25*, 307–320.

Burgisser, A., and G. W. Bergantz (2011), A rapid mechanism to remobilize and homogenize highly crystalline magma bodies, *Nature*, *471*, 212–215.

Caricchi, L., L. Burlini, P. Ulmer, T. Gerya, and P. P. M. Vassalli (2007), Non-newtonian rheology of crystal-bearing magmas and implications for magma ascent dynamics, *Earth Planet. Sci. Lett.*, *264*, 402–419.

Carman, P. C. (1937), Fluid flow through granular beds, *Trans. Inst. Chem. Eng.*, *15*, 150–166.

Costa, A. (2005), Viscosity of high crystal content melts: Dependence on solid fraction, *Geophys. Res. Lett.*, *32*, L22308, doi:10.1029/2005GL024303.

Couch, S., R. S. J. Sparks, and M. R. Carroll (2001), Mineral disequilibrium in lavas explained by convective self-mixing in open magma chambers, *Nature*, *411*, 1037–1039.

Davis, R. H., and K. H. Birdsell (1988), Hindered settling of semidilute monodisperse and polydisperse suspensions, *AIChE J.*, *34*, 123–129.

Davis, R. H., J. A. Schonberg, and J. M. Rallison (1989), The lubrication force between two viscous drops, *Phys. Fluids A*, *1*, 77–81.

Deubelbeiss, Y., B. J. P. Kaus, and J. A. D. Connolly (2010), Direct numerical simulation of two-phase flow: Effective rheology and flow patterns of particle suspensions, *Earth Planet. Sci. Lett.*, *290*, 1–12.

Forterre, Y., and O. Pouliquen (2008), Flows of dense granular media, *Annu. Rev. Fluid Mech.*, *40*, 1–24.

Geschwind, C. H., and M. J. Rutherford (1995), Crystallization of microlites during magma ascent: The fluid mechanics of 1980–1986 eruptions at Mount St Helens, *Bull. Volcanol.*, *57*, 356–370.

Ghiorso, M. S., M. M. Hirschmann, P. W. Reiners, and V. C. Kress III (2002), The pMELTS: A revision of MELTS for improved calculation of phase relations and major element partitioning related to partial melting of the mantle to 3 GPa, *Geochem. Geophys. Geosyst.*, *3*(5), 1030, doi:10.1029/2001GC000217.

Huber, C., O. Bachmann, and J. Dufek (2010), The limitations of melting on the reactivation of silicic mushes, *J. Veolcanol. Geotherm. Res.*, *195*, 97–105.

Huber, C., O. Bachmann, and J. Dufek (2011), Thermo-mechanical reactivation of locked crystal mushes: Melting-induced internal fracturing and assimilation processes in magmas, *Earth Planet. Sci. Lett.*, *304*, 443–454.

Huppert, H. E., and R. S. J. Sparks (1988), The generation of granitic magmas by intrusion of basalt into continental crust, *J. Petrol.*, *29*, 599–624.

Huppert, H. E., R. C. Kerr, J. R. Lister, and J. S. Turner (1991), Convection and particle entrainment driven by differential sedimentation, *J. Fluid Mech.*, *226*, 349–369.

Iga, K., and R. Kimura (2007), Convection driven by collective buoyancy of microbubbles, *Fluid Dyn. Res.*, *39*, 68–97.

Ishibashi, H. (2009), Non-Newtonian behavior of plagioclase-bearing basaltic magma: Subliquidus viscosity measurement of the 1707 basalt of Fuji volcano, Japan, *J. Volcanol. Geotherm. Res.*, *181*, 78–88.

Kaneko, K., and T. Koyaguchi (2000), Simultaneous crystallization and melting at both the roof and floor of crustal magma chambers: Experimental study using NH_4Cl-H_2O binary eutectic system, *J. Volcanol. Geotherm. Res.*, *96*, 161–174.

Kelemen, P. B., J. A. Whitehead, E. Aharonov, and K. A. Jordahl (1995), Experiments on flow focusing in soluble porous media, with applications to melt extraction from the mantle, *J. Geophys. Res.*, *100*, 475–496.

Koyaguchi, T., M. A. Halloworth, H. E. Huppert, and R. S. J. Sparks (1990), Sedimentation of particles from a convecting fluid, *Nature*, *343*, 447–450.

Krieger, I. M., and T. J. Dougherty (1959), A mechanism for Non-Newtonian flow in suspensions of rigid spheres, *Trans. Soc. Rheol.*, *3*, 137–153.

Leitch, A. M. (2004), Analog experiments on melting and contamination at the roof and walls of magma chambers, *J. Volcanol. Geotherm. Res.*, *129*, 173–197.

Lejeune, A., and P. Richet (1995), Rheology of crystal-bearing silicate melts: An experimental study at high viscosities, *J. Geophys. Res.*, *100*, 4215–4229.

Maaløe, S., and A. Scheie (1982), The permeability controlled accumulation of primary magma, *Contrib. Mineral. Petrol.*, *81*, 350–357.

Martin, D., and R. Nokes (1989), A fluid-dynamical study of crystal settling in convecting magmas, *J. Petrol.*, *30*, 1471–1500.

Masotta, M., C. Freda, and M. Gaeta (2012), Origin of crystal-poor, differentiated magmas: Insights from thermal gradient experiments, *Contrib. Mineral. Petrol.*, *163*, 49–65.

Mavko, G., T. Mukerji, and J. Dvorkin (1998), *The Rock Physics Handbook*, 329 pp., Cambridge Univ. Press, Cambridge, U. K.

McKenzie, D. (1984), The generation and compaction of partially molten rock, *J. Petrol.*, *25*, 713–765.

Michioka, H., and I. Sumita (2005), Rayleigh-Taylor instability of a particle packed viscous fluid: Implications for a solidifying magma, *Geophys. Res. Lett.*, *32*, L03309, doi:10.1029/2004GL021827.

Murphy, M. D., R. S. J. Sparks, J. Barclay, M. R. Carroll, and T. S. Brewer (2000), Remobilization of andesite magma by intrusion of mafic magma at the Soufriere Hills Volcano, Montserrat, West Indies, *J. Petrol.*, *41*, 21–42.

Nakada, S., and Y. Motomura (1999), Petrology of the 1991–1995 eruption at Unzen: Effusion pulsation and groundmass crystallization, *J. Volcanol. Geotherm. Res.*, *89*, 173–196.

Nakamura, M. (1995), Continuous mixing of crystal mush and replenished magma in the ongoing Unzen eruption, *Geology*, *23*, 807–810.

Olson, P., and D. Weeraratne (2008), Experiments on metal-silicate plumes and core formation, *Philos. Trans. R. Soc. A*, *366*, 4253–4271.

Onoda, G. Y., and E. G. Liniger (1990), Random loose packings of uniform spheres and the dilatancy onset, *Phys. Rev. Lett.*, *64*, 2727–2730.

Pallister, J. S., R. P. Hoblitt, and A. G. Reyes (1992), A basalt trigger for the 1991 eruptions of Pinatubo volcano?, *Nature*, *356*, 426–428.

Princen, H. M., M. P. Aronson, and J. C. Moser (1980), Highly concentrated emulsions II. Real systems. The effect of film thickness and contact angle on the volume fraction in creamed emulsions, *J. Colloid Interface Sci.*, *75*, 246–270.

Proussevitch, A. A., D. L. Sahagian, and A. T. Anderson (1993), Dynamics of diffusive bubble growth in magmas: Isothermal case, *J. Geophys. Res.*, *98*, 22,283–22,307.

Rabinowicz, M., P. Genthon, G. Ceulenner, and M. Hillairet (2001), Compaction in a mantle mush with high melt concentrations and the generation of magma chambers, *Earth Planet Sci. Lett.*, *188*, 313–328.

Saar, M. O., M. Manga, K. V. Cashman, and S. Fremouw (2001), Numerical models of the onset of yield strength in crystal-melt suspensions, *Earth Planet. Sci. Lett.*, *187*, 367–379.

Selig, F. (1965), A theoretical prediction of salt dome patterns, *Geophysics*, *30*, 633–643.

Takeuchi, S. (2011), Preeruptive magma viscosity: An important measure of magma eruptibility, *J. Geophys. Res.*, *116*, B10201, doi:10.1029/2011JB008243.

Thomas, N., S. Tait, and T. Koyaguchi (1993), Mixing of stratified liquids by the motion of gas bubbles: Application to magma mixing, *Earth Planet. Sci. Lett.*, *115*, 161–175.

Vinningland, J. L., O. Johnsen, E. G. Flekkoy, R. Toussaint, and K. J. Maloy (2007), Experiments and simulations of

a gravitational granular flow instability, *Phys. Rev. E*, *76*, 051306.

Voltz, C., W. Pesch, and I. Rehberg (2001), Rayleigh-Taylor instability in a sedimenting suspension, *Phys. Rev. E*, *65*, 011404.

Walsh, S. D., and M. O. Saar (2008), Numerical models of stiffness and yield stress growth in crystal-melt suspensions, *Earth Planet. Sci. Lett.*, *267*, 32–44.

Whitehead, J. A., and D. S. Luther (1975), Dynamics of laboratory diapir plume models, *J. Geophys. Res.*, *80*, 705–717.